

Tunable electromagnetically induced transparency in coupled three-dimensional split-ring-resonator metamaterials

Han, Song; Cong, Longqing; Lin, Hai; Xiao, Boxun; Yang, Helin; Singh, Ranjan

2016

Han, S., Cong, L., Lin, H., Xiao, B., Yang, H., & Singh, R. (2016). Tunable electromagnetically induced transparency in coupled three-dimensional split-ring-resonator metamaterials. *Scientific Reports*, 6, 20801-. doi: 10.1038/srep20801

<https://hdl.handle.net/10356/82744>

<https://doi.org/10.1038/srep20801>

© 2016 The Authors (Nature Publishing Group). This work is licensed under a Creative Commons Attribution 4.0 International License. The images or other third party material in this article are included in the article's Creative Commons license, unless indicated otherwise in the credit line; if the material is not included under the Creative Commons license, users will need to obtain permission from the license holder to reproduce the material. To view a copy of this license, visit <http://creativecommons.org/licenses/by/4.0/>

Downloaded on 25 Aug 2022 19:51:21 SGT

SCIENTIFIC REPORTS

OPEN

Tunable electromagnetically induced transparency in coupled three-dimensional split-ring-resonator metamaterials

Song Han¹, Longqing Cong^{2,3}, Hai Lin¹, Boxun Xiao⁴, Helin Yang¹ & Ranjan Singh^{2,3}

Received: 16 September 2015

Accepted: 12 January 2016

Published: 09 February 2016

Metamaterials have recently enabled coupling induced transparency due to interference effects in coupled subwavelength resonators. In this work, we present a three dimensional (3-D) metamaterial design with six-fold rotational symmetry that shows electromagnetically induced transparency with a strong polarization dependence to the incident electromagnetic wave due to the ultra-sharp resonance line width as a result of interaction between the constituent meta-atoms. However, when the six-fold rotationally symmetric unit cell design was re-arranged into a fourfold rotational symmetry, we observed the excitation of a polarization insensitive dual-band transparency. Thus, the 3-D split-ring resonators allow new schemes to observe single and multi-band classical analogues of electromagnetically induced transparencies that has huge potential applications in slowing down light, sensing modalities, and filtering functionalities either in the passive mode or the active mode where such effects could be tuned by integrating materials with dynamic properties.

Several fascinating properties of metamaterials occur due to electromagnetic coherent coupling between the induced oscillating currents at desired resonance frequencies. Electric as well as magnetic dipolar and high-order multipolar coupling are the commonly employed strategies to induce interference effects in subwavelength plasmonic and metamaterial resonators. These coupling effects between individual constituents play dominant roles in determining the optical properties of metamaterials. In nanostructures, a canonical method to harvest higher-order multipole is to construct plasmonic oligomers, such as disk/ring nanostructures^{2–4}, nanoparticle dimers^{5,6}, trimers⁷, tetramers^{8–10}, and some other high-order clusters^{11–16}. A hybridization process occurs when these nanoparticle clusters are excited by the incident light. It is the excitation of the multipoles that would induce a destructive interference (anti-bonding effect), which is a dominating approach to observe effects such as classical analog of electromagnetically induced transparency (EIT) phenomenon and the related Fano resonance phenomena^{4–18}. Alternatively, the anti-bonding effect between the induced electric dipole and the toroidal dipole has been used to observe the non-radiative resonant transparency¹⁹. Such a resonant transparency is non-trivial with the extremely high-Q resonances due to the low scattering of the electromagnetic field.

In this work, we exhibit the metamaterial coupling induced transparency in three-dimensional (3-D) split-ring resonators (SRRs) system that consists of three SRRs in a unit cell. We analyzed the transverse and longitudinal coupling in this system to understand the coherent coupling mechanism in the proposed structure. Detailed numerical simulations and an analytical coupled oscillator model were applied to reproduce the transparency spectra that would enhance the understanding of the underlying mechanism. The transparency window revealed a strong polarization-dependence behavior that reveals the switch-on and switch-off states with orthogonal polarization excitations. By re-arranging the polarization sensitive six-fold rotationally symmetric unit cells in a four-fold rotational symmetry configuration, we obtained a polarization insensitive transparency feature that exhibits dual-mode transparency windows.

¹College of physical science and technology, Central China Normal University, Wuhan 430079, China. ²Division of Physics and Applied Physics, School of Physical and Mathematical Sciences, Nanyang Technological University, Singapore 637371, Singapore. ³Centre for Disruptive Photonic Technologies, School of Physical and Mathematical Sciences, Nanyang Technological University, Singapore 637371, Singapore. ⁴Engineering Geophysical Research Center, Yangtze University, Jingzhou 434023, China. Correspondence and requests for materials should be addressed to H.Y. (email: emyang@mail.ccnu.edu.cn)

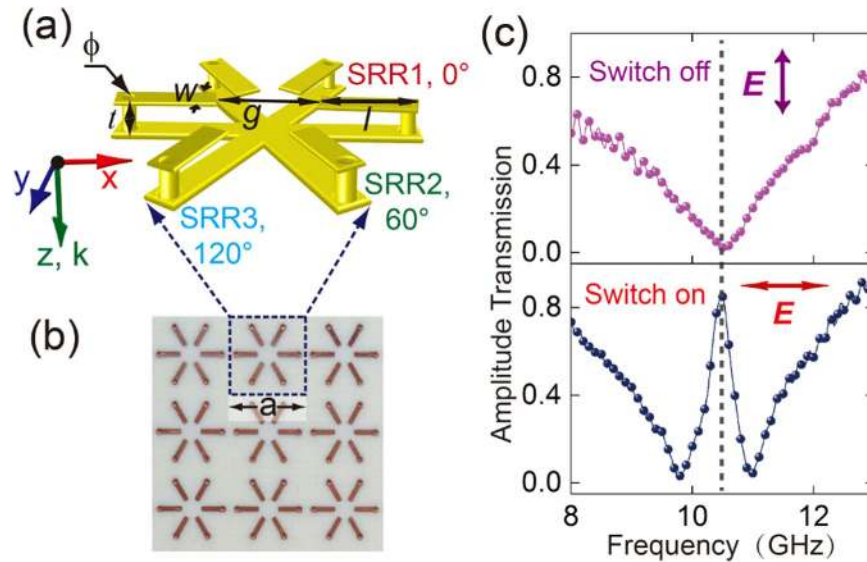


Figure 1. Metamaterial design and the measured spectra. (a) The unit cell consists of three SRRs, which is named as SRR1 (0°), SRR2 (60°) and SRR3 (120°), respectively. The specific geometrical parameters of each SRR are $w = 0.5$ mm, $l = 2.5$ mm, $g = 2$ mm, and $\phi = 0.4$ mm. (b) Top view of the experimental sample. The SRRs are supported by a dielectric substrate (Rogers RO4003) with the geometric dimensions of $a = 8$ mm, thickness $t = 0.813$ mm, and permittivity $\epsilon = 3.55$ with loss tangent of 0.0027. (c) The measured transmission spectra that reveal the on and off states for the transparency window. The arrows represent the incident polarization of the wave.

Results

We designed the 3-D metamaterial with a unit cell as shown in Fig. 1(a), where each SRR has a split gap on the top panel and a continuous wire in the bottom. In order to connect the top and bottom arms, two vertical metallic cylindrical pillars were fabricated to pierce through dielectric layer to form a three-dimensional SRR. The metal used in the design is Copper. It is well known that an oscillating current loop would be excited as the fundamental inductive-capacitive (LC) resonance mode by the incident electric field that polarized along the split gap or magnetic field that penetrates through the SRR. Under the 3-D configuration, the electric and magnetic fields would excite the mode in phase and we would consider electric field for simplicity. As shown in Fig. 1, the proposed metallic unit cell has six-fold (C6) rotational symmetry. However, this C6 symmetric unit cell with square periodicity on the dielectric substrate (C4 symmetry leads to the polarization-dependent property of the metamaterial (see Supplementary materials for details). Therefore, we define the horizontal polarized incidence as 0° (180°), i.e. the E-field is along x-direction, and the vertical polarized incidence as 90° , i.e. the E-field is along y-direction. At 90° polarized incidence, a broad resonance in the transmission spectrum is observed which is attributed to the fundamental resonance mode as shown in Fig. 1(c). However, when the polarization angle of incident light is rotated to 0° , a sharp transparency window with the transmission peak at 10.264 GHz is switched on.

In order to interpret the mechanism of the induced transparency window, we plot the simulated surface currents on the metallic structure as shown in Fig. 2(a). It is clearly observed that the oscillating currents are distributed on all the three SRRs for 0° polarized incidence at 10.264 GHz which interferes to form the transparency window in the spectrum. Since all the three SRRs are conductively connected through the bottom arms, the oscillating currents can be excited and induced in every SRR which gives rise to conductive coupling resulting in spectrum sharp transparency window. For the intermediate electric field polarization, the resonance is dominated by SRR1 when the angle lies between -30° to 30° . Therefore, SRR1 acts as a bright mode and SRR2, SRR3 are dark mode for this range of angles. Similarly, SRR2 dominates the resonance when the incident polarization angle lies between 30° to 90° , and SRR3, when the range is 90° to 150° (see Supplementary materials for details).

The oscillating currents on the metallic strips is equivalent to electric dipoles \mathbf{p} , and the loop currents induce magnetic dipoles \mathbf{m} as revealed in Fig 2(b). The electric-/magnetic-energy distributions at the transparent frequency presents hexapolar distribution feature that originates from the LC resonance nature of the structure: the electric energy accumulates at the gap of the SRRs while the magnetic energy is confined at the bottom strips of the SRRs. The electric (magnetic) dipoles plotted in Fig 2(b) present hybridized configuration, where the anti-bonding effect emerges when two oppositely arranged dipoles oscillate out of phase. The out of phase oscillating dipoles would destructively interfere which would tailor the resonant transparency band¹. The out-of-phase dipoles can be modeled as coupled oscillators^{19–22}:

$$\ddot{x}_1(t) + \gamma_1 \dot{x}_1(t) + \omega_0^2 x_1(t) + \Omega x_2(t) = gE \quad (1)$$

$$\ddot{x}_2(t) + \gamma_2 \dot{x}_2(t) + (\omega_0 + \delta) x_2(t) + \Omega x_1(t) = 0 \quad (2)$$

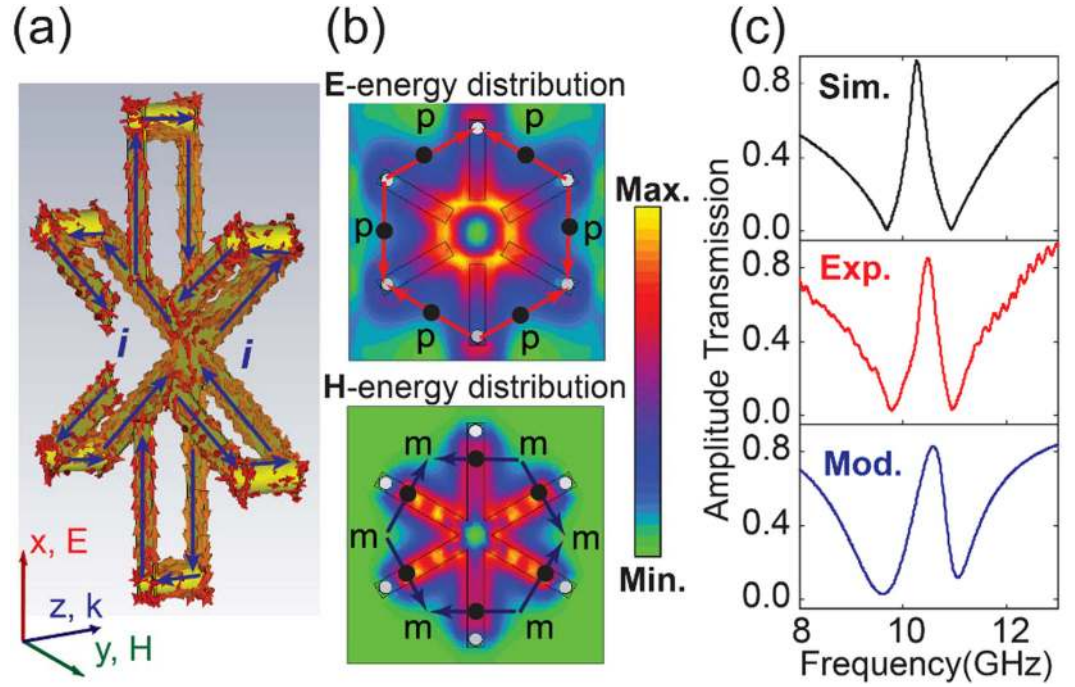


Figure 2. (a) The simulated surface currents at the transparent frequency, the blue arrows represent the currents on the front and back metallic strips, respectively. (b) The simulated E-energy and H-energy distribution where the equivalent electric dipoles (\mathbf{p}) and magnetic dipoles (\mathbf{m}) are artificially plotted according to the surface currents. (c) The simulated, measured and analytically calculated transmission spectra. For the analytical fit, we used the parameters of $\omega_0 = 9.68$ GHz, $\delta = 0.584$ GHz, $\gamma_1 = 2.439$ GHz, $\gamma_2 = 0.14$ GHz, $\Omega = 1.406$ GHz.

where (γ_1, γ_2) and (x_1, x_2) are the damping and the resonant amplitude of two oscillators, respectively. Oscillator 1 couples with the external field ($E = Ee^{i\omega t}$) through a coupling strength of g and oscillator 2 is a non-resonant mode with respect to the incident excitation, which can be coupled to the resonant mode (oscillator 1) through the near-field (conductive) coupling. The coupling between the two oscillators is described by the coupling strength of Ω . Considering that the radiative loss could be altered by connecting the SRRs together, we introduce a detuning factor δ that represents the frequency difference between the transparency frequency and the resonance frequency of oscillator 1. After solving the above coupled equations (1) and (2) with the displacements vectors expressed as $x_n = c_n e^{i\omega t}$ ($n = 1, 2$), and using the approximation of $\omega_1^2 - \omega^2 \approx -2\omega_1(\omega - \omega_1)^{21}$, the transmission as a function of frequency is obtained as

$$T = 1 - \text{Re} \frac{ig^2(\omega - \omega_0 - \delta + i\gamma_2/2)}{(\omega - \omega_0 + i\gamma_1/2)(\omega - \omega_0 - \delta + i\gamma_2/2) - \Omega^2/4} \quad (3)$$

Here we use the scattering parameters of an electric current sheet and the relation of $T = 1 - R^{22}$. The analytically fitted curve using equation 3 reveals a good agreement with the numerical simulation and the experimental results as shown in Fig. 2(c), which reflects the validity of the oscillator model.

Since the unit cell is polarization-dependent due to the six-fold rotational symmetry (C6), the metamaterial shows an anisotropic behavior. We therefore investigated the transmission behavior of the 3-D metamaterial at varied incident polarization angles. As shown in Fig. 3, the corresponding results at various incident polarization vectors clearly reveal that the amplitude of the transparent window is gradually modulated as the polarization angle is varied from 0° to 90° . Simulation and experiment results reveal an excellent agreement by comparing the spectra. In addition, by tailoring parameters (γ_1, γ_2) , ω_0 , δ , and Ω in the coupling model discussed above (see Supplementary materials for details), the modulation behavior of transmission spectra was reproduced in the third column shown in Fig. 3. The measured, simulated and the analytically calculated data reveal the gradual modulation of the transparency window from “on” to “off” state with varied polarization vector direction. According to the coupling model, the radiative loss γ_1 , the detuning δ and the coupling strength Ω between two oscillators are tuned while rotating the incident polarization vector angle from 0° to 90° , where the coupling strength Ω gradually decreases. For the case when the transparency phenomena disappears (90° polarized incidence), Ω is equal to zero which indicates the dependence of coupling strength Ω on the polarization angles that causes the modulation of the transparency band.

To visualize the interplay of the scattered near-fields under different incident polarization vectors, we simulated the electric and magnetic energy distributions for varied incident polarization vector as shown in Fig. 4. As we can observe, the electric and magnetic energy is distributed on the three SRRs due to their near-field interaction that results in the transparency window at cases of 0° and 70° polarization and the intensity reveals

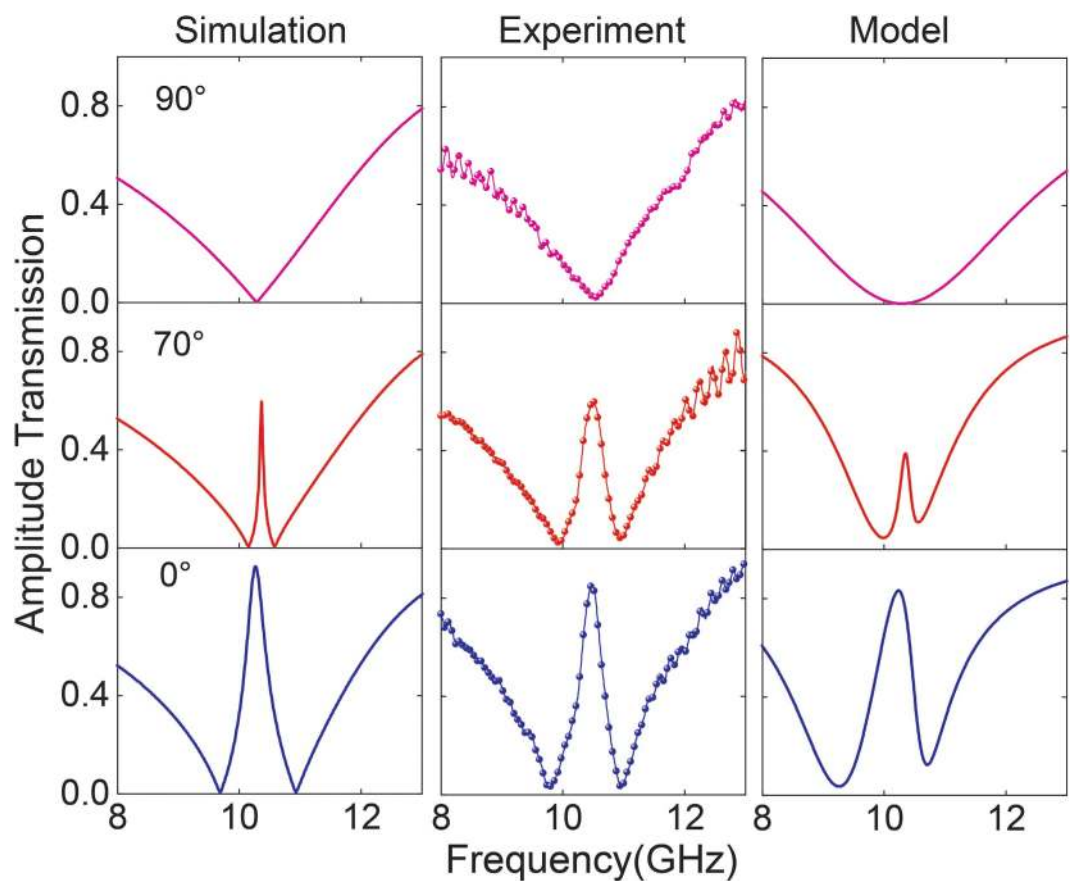


Figure 3. The simulated, measured and analytically modelled transmission spectra at different incident polarization angles.

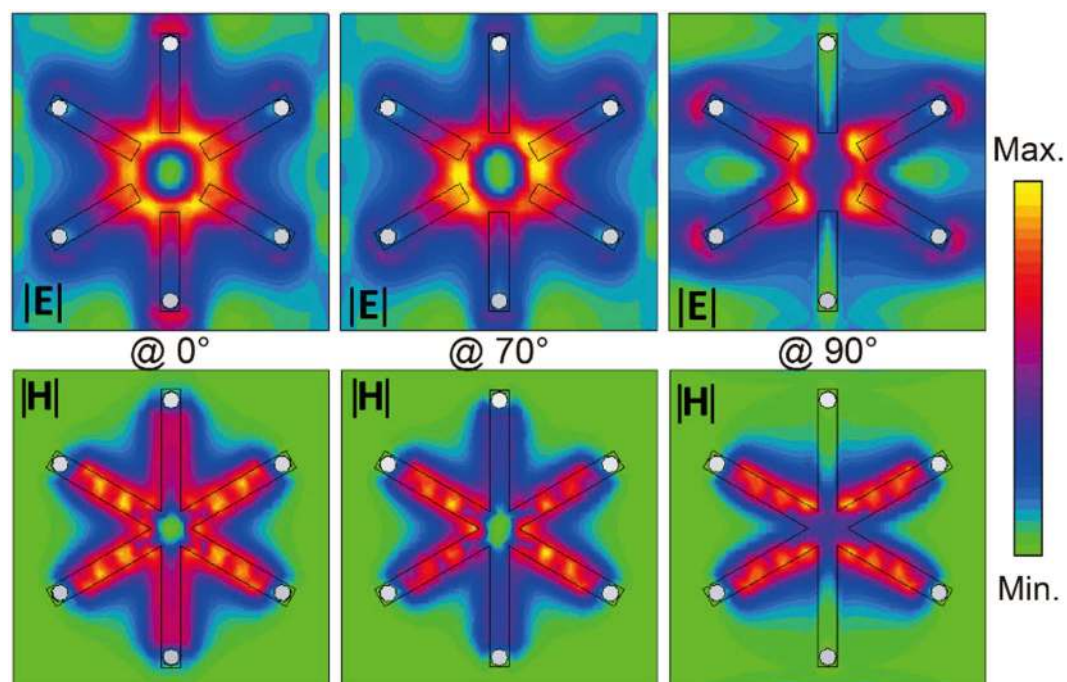


Figure 4. The electric and magnetic field energy distribution at the incident polarization angle of 0° , 70° and 90° , (see Supplementary materials for details).

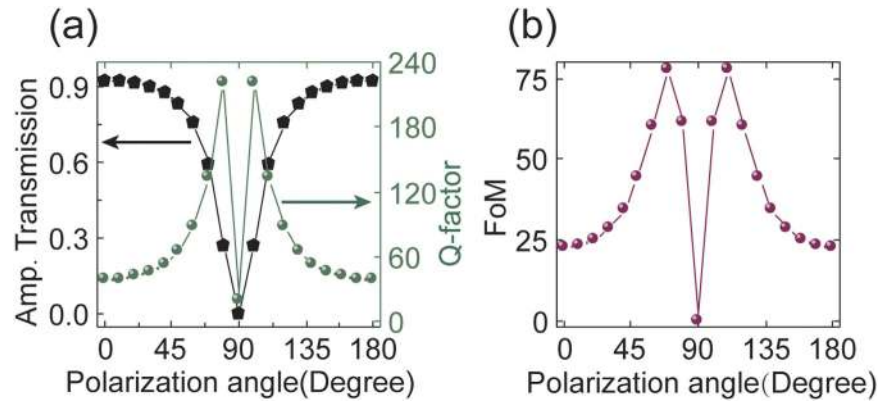


Figure 5. (a) Amplitude transmission and the Q-factor and (b) the FoM of the transparency band at different incident polarization angle.

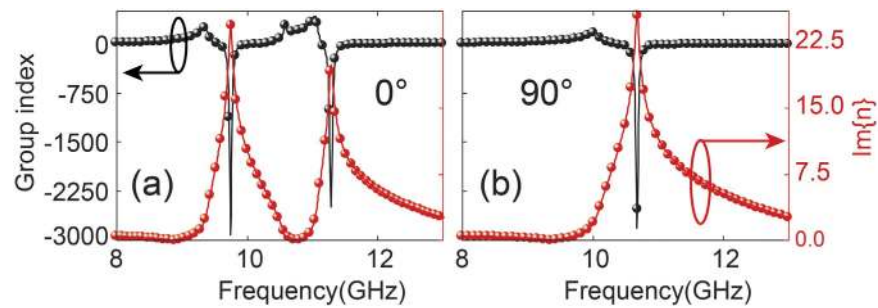


Figure 6. The real part of the group index (n_g) and the imaginary part of the index of refraction [$\text{Im}(n)$] as a function of frequency. The incident polarization angle is (a) 0° and (b) 90° .

the modulation of the transparency while the field distribution is only concentrated on SRR2 and SRR3 at 90° polarization. In fact, SRR1 dominates the resonance at 0° polarization incidence where SRR1 gets excited and couples to SRR2 and SRR3 thereby forming anti-bonding dipoles that gives rise to the transparency. With the rotation of the excitation vector to 70° , the resonance is gradually dominated by SRR2 so that SRR2 couples with SRR1 and SRR3, and thereby give rise to transparency induced by near-field anti-bonding effect. However, the electric and magnetic energy distribution on SRR1 disappears when the incident polarization angle is 90° . Under this situation, SRR1 is completely uncoupled to external excitation field. In addition, SRR1 is also uncoupled to SRR2 and SRR3 where we can treat SRR2 and SRR3 as an effective SRR that is perpendicular to SRR1 so that the metamaterial shows the opacity at the 90° incident polarization angle. By rotating the incident polarization vector, both the electric and magnetic energy distributions demonstrate that the near-field interaction in three SRRs dampens gradually, i.e. the coupling strength Ω in coupled oscillator model becomes weaker, which leads to the modulation of the transparency window.

Discussion

The transparency window reveals a very sharp line shape which offers the avenue for applications in light-matter interactive systems such as a sensing or a slow light device. In order to give a numerical description of the transparency in terms of the resonance linewidth and its intensity, we show the Q-factor and the figure of merit (FoM) obtained through rigorous simulations in Fig. 5. From the figures, we can clearly observe that the amplitude of the transparency window is modulated while rotating the polarization vector and at the same time, the quality factor (Q) also changes, as shown in Fig. 5(a). In order to find the trade-off between the Q factor and the amplitude of the transparency window, the FoM is defined as $\text{FoM} = A \cdot Q$, where A is the transmission amplitude and Q is the quality factor of the transparency window²³. At around 60° (120°) of the polarization vector, we can observe the optimal FoM value that attains a high value of 77 (see in Fig. 5(b)) with the Q factor of 130.3 and amplitude of 0.595 (see in Fig. 5(a)). Such a high value of FoM indicates that the proposed metamaterial can be applied as high Q-factor tunable filter and ultrasensitive sensing devices^{22–26}.

In order to clearly understand the slow light effect of the proposed metamaterial, the group index as a function of frequency, i.e., $n_g = n + \omega \frac{dn}{d\omega}$, where n is the effective refractive index (see Supplementary Materials for details) of the metamaterial and ω is the frequency of light, can be used to depict this slow light property. Figure 6(a) presents the calculated group index (n_g) of the proposed metamaterial at the polarization angle of 0° , where the real part of the group index is observed to reveal a large value (up to 427) within the frequency regime of the transparent window. The time delay is calculated as $\tau = \frac{d(n_g - n)}{c}$, where d is the thickness of the substrate (Rogers

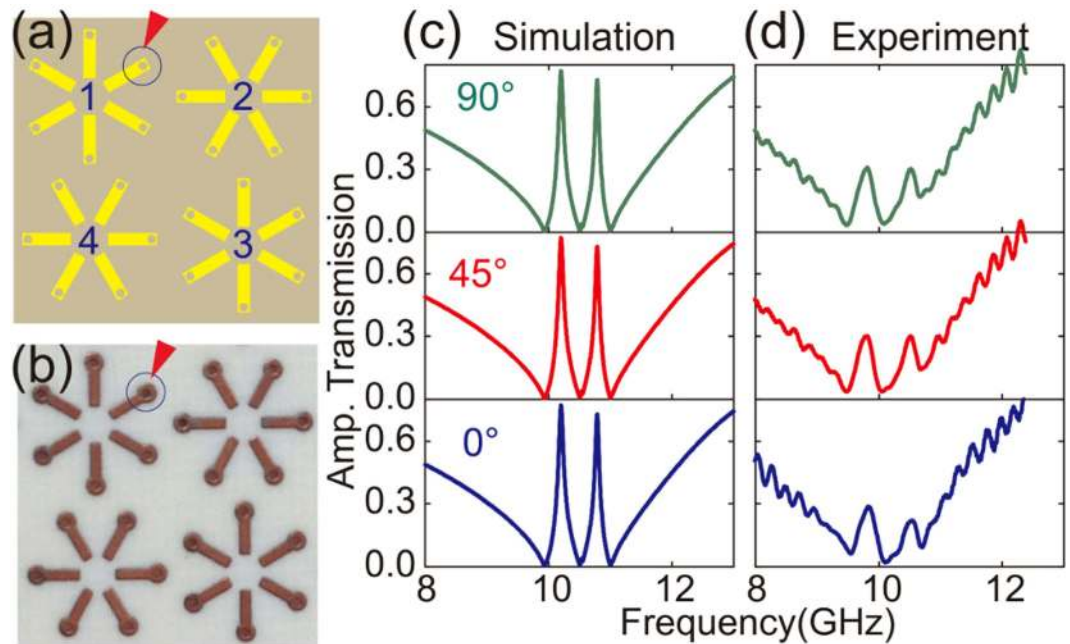


Figure 7. Four-fold (C_4) rotationally symmetric unit cells with orthogonally twisted meta-atoms 1, 2, 3 and 4 are shown in (a) artistic and (b) fabricated version, respectively. Simulated (c) and experimental (d) results present dual-mode polarization-independent transparencies.

RO4003) and c is the speed of light in vacuum. Therefore, the calculated time delay is up to 1.19 ns within the transparent band. The giant group index at the transparent range shows that the proposed metamaterial can slow down the propagating EM waves efficiently²². For comparison, the calculated group index (n_g) at 90° polarization angle is also shown in Fig. 6(b), where the group index disappears and reveals a giant dip at the transmission minima. According to the time delay calculation, the slow light effect disappears at 90° polarization angle. The imaginary part of the refractive index is also calculated as shown in Fig. 6(a), where almost a near zero value is observed at the transparent frequency. However, we see two very strong peaks at the transmission dips, which implies that the incident light was transmitted with smaller loss in the transparency range and strongly scattered and absorbed by the material at the two transmission dips.

As we have demonstrated, the proposed 3-D design can switch the transparency window from “on” to “off” state with varied polarization vectors that manifests the feature of polarization dependent EIT behavior. However, the polarization insensitivity could also be realized by re-designing the unit cell to preserve the intrinsic C_4 symmetry. We introduce four resonators in a unit cell with a C_4 symmetry^{26–29} as shown in Fig. 7(a,b). We experimentally as well as numerically probed the transmission spectra under such a configuration which is displayed in Fig. 7(c,d). The simulated and the corresponding measured transmission spectra exhibit similar transmission behavior with vertically (0°), diagonally (45°) and horizontally (90°) polarized incident waves, demonstrating the polarization independence. Additionally, the transmission spectra shows a pronounced dual-mode transparency window. The dual-mode transparency could be understood if we re-examine the hybrid unit cell of the metamaterial structure. The new pattern consists of a layout where the diagonal resonator pair in the unit cell is mutually twisted by 90° . In this new design, the two transparent windows originate from the nearest neighbor coupling among the four meta-atoms in the unit cell. As we discussed previously, the transparency windows of meta-atom 1 and 3 are switched on with high Q -factor at 0° polarization incidence, but those of meta-atom 2 and 4 are switched off which leads to a low Q -factor resonance. With the intra meta-atom coupling under the 0° polarization excitation, mode interference between the meta-atoms results in two transparency windows in the spectra as shown in Fig. 7(c). This implies that the diagonally arranged metamaterial support destructive interference through the nearest neighbor coupling^{30–32}. As a result, the new arrangement of meta-atoms (C_4 symmetry) demonstrates a dual-mode transparency. For the case of 90° incidence, the meta-atom 2 and 4 are switched on and meta-atom 1 and 3 are switched off, which would support the same interference spectra. For the incident angle from 0° to 45° , meta-atom 1 and 3 support low- Q EIT and meta-atom 2 and 4 support high- Q EIT. However, they could interfere with each other through nearest neighbor coupling. Therefore, the high- Q transparent spectrum (atoms 2 and 4) overlaps with the low- Q spectrum (atoms 1 and 3) and gives rise to the dual-mode EIT phenomena. Similar arguments could be applied for the incident angles varying from 45° to 90° . Some mismatch between the measured and the simulated data appear in Fig. 7, which mainly originates from the low quality of perforated joints as indicated by the red triangle in Fig. 7(a).

In summary, we have experimentally and numerically provided a novel design scheme using three dimensional metamaterial structures that support classical analog of electromagnetically induced transparency and slow light behavior. The spectral features and the underlying physics are explained by using the anti-bonding mode of hybridized electric-/magnetic-dipoles. The coupling between hybridized dipoles can be understood in

terms of the coupled oscillator model, which shows the destructive interference based transparency in the chosen metamaterial design. The six-fold rotationally symmetric structure demonstrated in this work showed polarization dependent modulation of the metamaterial induced transparency window. However, by re-arranging the meta-atoms into a four-fold rotational symmetry in the unit cell, we could achieve polarization independent dual-mode transparency. We believe that the three dimensional metamaterial design presented in this work will play an important role in extending the multifunctional device applications, such as optical switches, high-Q tunable band-pass single mode and multimode filters, frequency selective devices, optical modulators, and ultra-sensitive sensors^{33–35}.

Methods

The full-wave numerical simulation software CST microwave studio was employed to analyze the spectral response. Open boundary conditions were set along the light propagating direction (z-direction), and unit cell boundary conditions were applied at the x-y plane. After optimizing the parameters in simulations, experimental samples with overall dimension of $200 \times 200 \text{ mm}^2$ were fabricated using the printed circuit board (PCB) technique, whose images of top and bottom panel are shown in Fig. 1(b). The spectral responses were measured by two linearly polarized horn antennas used as an emitter and a receiver. A vector network analyzer (Agilent N8362B) was employed to store and retrieve data.

References

1. F. Hao *et al.* Tunability of Subradiant Dipolar and Fano-type Plasmon Resonances in Metallic Ring/Disk Cavities: Implications for Nanoscale Optical Sensing, *ACS. NANO*, **3**, 643–652 (2009).
2. Y. H. Fu *et al.* Generating and Manipulating Higher Order Fano Resonances in Dual-Disk Ring Plasmonic Nanostructures, *ACS. NANO*, **6**, 5130–5137 (2012).
3. Y. Zhang *et al.* Fano resonances in disk–ring plasmonic nanostructure: strong interaction between bright dipolar and dark multipolar mode, *Opt. Lett.* **37**, 4919–4921 (2012).
4. L. V. Brown *et al.* Heterodimers: Plasmonic Properties of Mismatched Nanoparticle Pairs, *ACS NANO*, **4**, 819–832 (2010).
5. K. C. Woo *et al.* Universal Scaling and Fano Resonance in the Plasmon Coupling between Gold Nanorods, *ACS. NANO*, **5**, 5976–5986 (2011).
6. S. N. Sheikholeslami *et al.* Controlling the Interplay of Electric and Magnetic Modes via Fano-like Plasmon Resonances, *Nano Lett.* **11**, 3927–3943 (2011).
7. J. A. Fan *et al.* Fano-like Interference in Self-Assembled Plasmonic Quadramer Cluster, *Nano Lett.* **10**, 4680–4685 (2010).
8. J. Sancho-Parramon & S. Bosch. Dark Modes and Fano Resonances in Plasmonic Clusters Excited by Cylindrical Vector Beams, *ACS. NANO*, **6**, 8415–8423 (2012).
9. M. Rahmani *et al.* Subgroup Decomposition of Plasmonic Resonances in Hybrid Oligomers: Modeling the Resonance Lineshape, *Nano Lett.* **12**, 2101–2106 (2012).
10. M. Hentschel *et al.* Transition from Isolated to Collective Modes in Plasmonic Oligomers, *Nano Lett.* **10**, 2721–2726 (2010).
11. J. B. Lassiter *et al.* Fano Resonances in Plasmonic Nanoclusters: Geometrical and Chemical Tunability, *Nano Lett.* **10**, 3184–3189 (2010).
12. D. Dregely, M. Hentschel & H. Giessen. Excitation and Tuning of Higher-Order Fano Resonances in Plasmonic Oligomer Clusters, *ACS. NANO*, **10**, 8202–8211 (2011).
13. J. A. Fan *et al.* Near-Normal Incidence Dark-Field Microscopy: Applications to Nanoplasmonic Spectroscopy, *Nano Lett.* **12**, 2817–2821 (2012).
14. A. E. Miroshnichenko & Y. S. Kivshar Fano Resonances in All-Dielectric Oligomers, *Nano Lett.* **12**, 6459–6463 (2012).
15. K. Thyagarajan, J. Butet & O. J. F. Martin. Augmenting Second Harmonic Generation Using Fano Resonances in Plasmonic Systems, *Nano Lett.* **13**, 1847–1851 (2012).
16. E. Heinrich-Josties, S. Pabst & R. Santra. Controlling the 2p hole alignment in neon via the 2s–3p Fano resonance, *Phys. Rev. A* **89**, 043415 (2014).
17. R. Gupta, Q. Xiong *et al.* Laser-Induced Fano Resonance Scattering in Silicon Nanowires, *Nano. Lett.* **3**, 627–631 (2003).
18. Y. S. Joe, A. M. Satanin & C. S. Kim. Classical analogy of Fano resonances, *Phys. Scr.* **74**, 259–266 (2006).
19. V. A. Fedotov *et al.* Resonant Transparency and Non-Trivial Non-Radiating Excitations in Toroidal Metamaterials, *Sci. Rep.* **3**, 2967 (2013).
20. N. Liu *et al.* Planar metamaterial analogue of electromagnetically induced transparency for plasmonic sensing, *Nano Lett.* **10**, 1103 (2010).
21. N. Liu *et al.* Plasmonic analogue of electromagnetically induced transparency at the Drude damping limit, *Nat. Mater.* **8**, 758 (2009).
22. P. Tassin *et al.* Low-loss metamaterials based on classical electromagnetically induced transparency, *Phys. Rev. Lett.* **102**, 053901 (2009).
23. L. Q. Cong *et al.* Fano Resonances in Terahertz Metasurfaces: A Figure of Merit Optimization. *Adv. Optical Mater.* **3**, 1537 (2015).
24. J. Q. Gu, R. Singh *et al.* Active control of electromagnetically induced transparency analogue in terahertz metamaterials, *Nat. Commun.* **3**, 1151 (2012).
25. R. Singh *et al.* Ultrasensitive terahertz sensing with high-Q Fano resonances in metasurface, *Appl. Phys. Lett.* **105**, 107101 (2014).
26. W. Zhou *et al.* Progress in 2D photonic crystal Fano resonance photonics, *Progress in Quantum Electronics*, **38**, 1–74 (2014).
27. X.-Q. Zhang *et al.* Polarization-independent plasma-induced transparency in a fourfold symmetric terahertz metamaterial. *IEEE J.* **19**, 8400707 (2013).
28. S. Han & H.-L. Yang. Study on the design and measurement of dual-directional multi-band metamaterial absorber. *Acta. Phys. Sin. (Chinese edition)* **62**, 174102 (2013).
29. H.-Y. Shi *et al.* Dual-band polarization angle independent 90° polarization rotator using twisted electric-field-coupled resonators. *Appl. Phys. Lett.* **104**, 034102 (2014).
30. D. R. Chowdhury *et al.* Tailored resonator coupling for modifying the terahertz metamaterial response. *Opt. Express* **19**, 10679 (2011).
31. W. Cao, R. Singh *et al.* Plasmon-induced transparency in metamaterials: Active near field coupling between bright superconducting and dark metallic mode resonators. *Appl. Phys. Lett.* **103**, 101106 (2013).
32. R. Singh, I. Al-Naib *et al.* Probing the transition from an uncoupled to a strong near-field coupled regime between bright and dark mode resonators in metasurfaces. *Appl. Phys. Lett.* **105**, 081108 (2014).
33. R. Singh *et al.* The Fano Resonance in Symmetry Broken Terahertz Metamaterials. *Terahertz Science and Technology, IEEE Transactions on* **3**, 820 (2013).
34. L.-Q. Cong, S. Y. Tan *et al.* Experimental demonstration of ultrasensitive sensing with terahertz metamaterial absorbers: A comparison with the metasurfaces. *Appl. Phys. Lett.* **106**, 031107 (2015).
35. M. Manjappa *et al.* Tailoring the slow light behavior in terahertz metasurfaces. *Appl. Phys. Lett.* **106**, 181101 (2015).

Acknowledgements

S.H., H.Y. and B.X. acknowledge National Natural Science Foundation of China Grant No. 41474117 for funding of this research. L.C. and R.S. acknowledge NTU startup Grant No. M4081282, MoE Tier 1 Grant No. M401136, and MOE grant No. MOE2011-T3-1-005 for funding of this research.

Author Contributions

S.H. initializes the idea and performs the numerical calculation, S.H., H.L. and H.Y. perform experimental measurements, S.H., L.C. and R.S. performs the theoretical analysis, H.Y. and B.X. supervise the project, S.H., L.C. and R.S. wrote the manuscript, and all authors discuss the results.

Additional Information

Supplementary information accompanies this paper at <http://www.nature.com/srep>

Competing financial interests: The authors declare no competing financial interests.

How to cite this article: Han, S. *et al.* Tunable electromagnetically induced transparency in coupled three-dimensional split-ring-resonator metamaterials. *Sci. Rep.* **6**, 20801; doi: 10.1038/srep20801 (2016).



This work is licensed under a Creative Commons Attribution 4.0 International License. The images or other third party material in this article are included in the article's Creative Commons license, unless indicated otherwise in the credit line; if the material is not included under the Creative Commons license, users will need to obtain permission from the license holder to reproduce the material. To view a copy of this license, visit <http://creativecommons.org/licenses/by/4.0/>